CrossMark

Multifractal analysis of Hg pore size distributions of tectonically deformed coals

Wei Li, Hongfu Liu *, Xiaoxia Song

Department of Earth Science and Engineering, Taiyuan University of Technology, Taiyuan 030024, PR China

ARTICLE INFO

ABSTRACT

To get deep insight into the variability and heterogeneity of pore size distributions (PSDs) in different tectonically deformed coals (TDCs) (mean maximum vitrinite reflectance $R_{o,max}$ ranging from 1.720% to 1.857%) collected from Hancheng Mine, Weibei coalfield, the multifractal analysis using generalized dimensions D_q was employed to study PSDs of TDCs based on mercury intrusion porosimetry. The mercury intrusion data under pressure over 10 MPa was corrected in combination with gas adsorption data. The results show that, for the test coals, tectonic deformation (TD) mainly increases seepage-porosity while maceral composition (MC) is the main control on adsorption-porosity. The variations of D_q versus q show that the PSDs of TDCs exhibit multifractal behavior, however, differ in their multifractality suggested by the extracted parameters from PSDs including information dimension D_1, the Hurst exponent H, the width of the right side $D_0–D_{10}$ and the left side $D_{-10}–D_0$ of D_q spectra. TD and MC have great influence on the variability and heterogeneity in the inner distribution of seepage-porosity and adsorption-porosity respectively, as demonstrated by the change of D_1, H and $D_0–D_{10}$ for moment $q > 0$ and $D_{-10}–D_0$ for moment $q < 0$. Both D_1 and H increase with TD but $D_0–D_{10}$ shows a reverse trend. Consequently, TD leads to narrower distribution with higher fluctuation, lower pore connectivity and greater complexity in the distribution of seepage-pores, which may be due to the presence and uneven distribution of microfracture and inter-granular pores formed through deformation process. Increasing vitrinite and decreasing inertinite contribute to a heterogeneous distribution of adsorption-porosity, as observed by the high correlation between $D_{-10}–D_0$ and MC. The aforementioned results confirm that the multifractal approach is useful to characterize the internal heterogeneity of PSDs and to detailedly distinguish between PSDs of TDCs.

1. Introduction

The pore size distributions (PSDs) of coals have gained wide attention since they have a significant influence on the success of exploiting coalbed methane (CBM) from wells (Clarkson and Bustin, 1999; Zhang et al., 2013a, 2013b). The pore properties are related to the complex physical and chemical structures of coals (Bustin et al., 1995; Firouzi et al., 2014; Xu et al., 2014). The flow property and storage capacity of gas in coals vary due to the heterogeneous textural structure of coals.

Tectonically deformed coals (TDCs) were formed under tectonic movements, and its primary structure, physical and chemical texture were changed (Hou et al., 2012). Coal basins in China have complex tectonic evolutionary histories (Liu et al., 2000), and thus it results in strong transformation of coal structure and various TDCs, which might induce changes in physical properties of CBM reservoirs (Beamish and Crosdale, 1998; Cao et al., 2003). Under tectonic deformation, the PSDs have changed, resulting in different gas transportation and adsorption behavior and providing new insight into CBM recovery in deformed coalbeds (Hou et al., 2012; Li et al., 2003). Therefore, a full elaboration of the PSDs of TDCs will be favorable for CBM recovery and coal and gas outbursts prediction.

Various methods were used to study PSDs of coals. Statistical descriptions of the PSDs can be inferred indirectly from mercury intrusion porosimetry (MIP) (Yao and Liu, 2012; Zou et al., 2013), small-angle scattering (Radliński et al., 2004) and gas adsorption analyses (Bae et al., 2009). Direct observational methods such as scanning electron microscopy (SEM) (Giffin et al., 2013), microfocus X-ray computed tomography (μCT) (Golab et al., 2013; Kumar et al., 2011) and atomic force microscope (AFM) (Lawrie et al., 1997; Wu et al., 2014) permit quantification of pore properties including porosity, pore size and connectivity on two- and three-dimensional views. Among these, MIP is frequently used to estimate PSDs and has been used to characterize pore size of TDCs (Qu et al., 2010). The MIP method is useful for characterizing porosity distribution with pore size above 3 nm (Gan et al., 1972; Ritter and Drake, 1945), but the high pressure (P > 10 MPa) may damage narrow pores or compress the coal matrix, and the

* Corresponding author at: Huyu Campus, Taiyuan University of Technology, No. 18, New Kuangyuan Road, Wanbailin District, Taiyuan City, Shanxi Province, PR China. Tel./fax: +86 351 6018950.
E-mail address: lhftyut@163.com (H. Liu).

reduction in bulk volume of the sample could occur (Friesen and Mikula, 1988). With the applied pressure increasing, the simultaneous compression and pore-filling occur during mercury intrusion (Li et al., 1999). Thus, prior to characterization of the PSDs by using MIP data, the effects of coal compressibility at pressure over 10 MPa should be carefully examined and corrected, and then the corrected Hg pore volume can be used to characterize PSDs for coals (Cai et al., 2013; Gökhan Şenel et al, 2001). However, the mercury intrusion data correction has not been carried out in the evaluation of PSDs related to TDCs, which would lead to an erroneous result for pore volume evaluation without compressibility correction. Furthermore, the compressibility of coal used to adjust the Hg pore volume is difficult to determine using the MIP method alone (Friesen and Mikula, 1988). N_2 adsorption is useful for characterizing porosity in the pore size range of 2–300 nm (Gan et al., 1972; Unsworth et al., 1989), and CO_2 adsorption works well for characterizing micro-porosity (<2 nm) (Liu and Wilcox, 2013; Mastalerz et al., 2008). In this work, N_2 adsorption data were used to characterize the pore-filling volume measured by MIP in the high pressure interval. In combination with MIP data and N_2 and CO_2 adsorption data, the compressibility of seven typical TDCs was determined and the Hg pore volume was adjusted based on the work of Li et al. (1999). The PSDs related to coal deformation structures after Hg data correction were further discussed.

The pore sizes of coals are not uniformly distributed in space, which makes it difficult to characterize the complexity of PSDs by traditional Euclidean geometry. In that case, fractals, initially proposed by Mandelbrot (1967), have been widely used to quantitatively characterize physical properties of spatially non-uniform systems and one parameter, the fractal dimension, D, has been introduced to describe the irregular distribution of pore sizes of coals (Gauden et al., 2001; Yao et al., 2009a). However, the profiles of the distribution of pore sizes of coals often show "fluctuations" and "jumps" at different pore size intervals and, in general, types of erratic variation or local variation occur in the inner distribution of pore sizes which cannot be explained by a single-scale (monofractal) analysis or a single fractal dimension. In fact, for irregular distribution of pore sizes of coals, a single fractal dimension would describe the irregularity within limited size intervals, that is, different pore size intervals would show different types of self-similarity (Friesen and Mikula, 1987; Li et al., 1999). These characteristics can also be found in many non-uniform PSDs in nature which can be described as multifractal structure (Muller and McCauley, 1992). These complex distributions can be attributed to the underlying nonlinear dynamics, as superposition of different processes acting simultaneously along a wide range of length scale (Peitgen et al., 1992). Studies have shown that the variation and distribution of pore sizes for porous media can be assigned to an underlying nonlinear dynamics system, and multifractal analysis seems to be an appropriate tool to analyze the inner non-linear variation or heterogeneous distribution of pore sizes for porous media (Caniego et al., 2003; Muller, 1996; San José Martínez et al., 2010).

Multifractals can be treated as an extension of fractals. Indeed, a multifractal structure is considered as a superposition of monofractal structure (Posadas et al., 2003). In comparison of monofractal structure, the multifractal structure can be decomposed into a set of intertwined fractal subsets demonstrated by a hierarchy of scaling exponents that characterize the local variability and heterogeneity of studied variables (Kravchenko et al., 1999). The multifractal analysis captures the inner variations in a system by resolving local densities (probability) and expresses them by a continuous of fractal dimensions spectrum referred to as singularity spectrum and generalized dimension spectrum (Chhabra et al., 1989). In view of this, the multifractal approach has been successfully applied to characterize the inner variation of PSDs in soil (Montero and Martín, 2003) and sedimentary rocks (Anovitz et al., 2013; Cheng, 1999). Several authors carried out multifractal studies of PSDs of porous material from image analysis. San José Martínez et al. (2010) performed the multifractal analysis of soil macropore structure at horizon scale

using X-ray computed tomography (CT) data. It was found that the multifractal approach is an effective tool for parameterizing the spatial heterogeneity of soil macropore structure. Muller and McCauley (1992) first used the idea of multifractal scaling to characterize the PSDs in sedimentary rocks through an optical microscope. They demonstrated how the multifractal scaling of pore space can be used as a tool for rock characterization. Xie et al. (2010) investigated the multifractal analysis of porosity of sedimentary carbonate from two-dimensional environmental scanning electron microscope (ESEM) image. They observed that the reservoir capacity assessment result derived from multifractal analysis is consistent with the field research. Recently, multifractal analysis of PSDs determined by MIP method has been performed (Paz Ferreiro and Vidal Vázquez, 2010). Sanjurjo-Sánchez and Vidal Vázquez (2013) assessed the surface weathering of a granite rock by combination of elemental chemical analysis and multifractal analysis of Hg injection data sets. They found that multifractal parameters of PSDs are suitable indicator for evaluating weathering. From the above literature review, it is found that multifractal analysis of PSDs measured by Hg injection in TDCs has not been performed.

In this work, we use the multifractal approach to investigate the variability and heterogeneity of PSDs in different TDCs with Hg pore volume–size data after compressibility correction and to determine whether multifractal parameters can be used to compare the variability of PSDs in different TDCs with similar coal rank. The quantitative characterization of PSDs based on multifractal analysis may provide relevant information which can be used to improve our understanding how tectonic deformation affects PSDs in coal.

According to the work of Unsworth et al. (1989) and Cai et al. (2013), a combined pore classification from Hodot (1961) and IUPAC (Sing et al., 1985) is employed in this study: microfracture ($d > 10,000$ nm), macropore (1000 nm $< d < 10,000$ nm), mesopore (100 nm $< d < 1000$ nm), transition pore (10 nm $< d < 100$ nm), micropore (2 nm $< d < 10$ nm), and super-micropore ($d < 2$ nm), where d is the pore diameter. Based on the interaction of gas molecular and pore size, macropore and mesopore are called seepage–pore, where gas laminar flow occur during production, while transition pore, micropore and super-micropore are assigned to adsorption–pore in which gas diffusion and physical adsorption occur (Shi and Durucan, 2005). Among these pores, the super-micropore plays a dominant role in gas adsorption (Mastalerz et al., 2008).

2. Geological setting

The Hancheng mining district (HMD) is located in the southeastern margin of Ordos Basin. Structurally, it is a monoclinal structure, northwest trend, southeast dip with 5°–10°. The district experienced three big tectonic events including the Indo-Chinese, Yanshanian and Himalayan periods. Gentle fold with the axis trending EW–NWW formed under SSW–NNE compression during the Indosinian stage. The fold and thrust faults striking NE formed under intensive SE–NW compression during the Yanshanian stage. The HMD suffered S–N and SE–NW extension under NWW compression during the Himalayan stage (Yao et al., 2009b). The regional structures in HMD possess strong structure in east and south and weak structure in north and west due to the effect of multiple tectonic deformation (Fig. 1a). The strong tectonic deformation is concentrated in the southeastern margin of the district. Two sets of structure are well developed in Hangcheng mining area: one set strikes NNE–NE, such as F1 normal fault located in the eastern margin, another set strikes NEE, including Longting, Dongzecun and Longguling tectonic belt from south to north (Fig. 1a).

Based on the distribution of structures in HMD, the dominant structure in Shangshuping (SSP) coalmine located in the north of HMD is compressional fold and the collected samples in SSP are located in the axial part of syncline (Fig. 1a). The structure in Xiangshan (XS) coalmine located in the south of HMD shows somewhat complicated. The small-scale bed-parallel compressional faults are developed and the collected
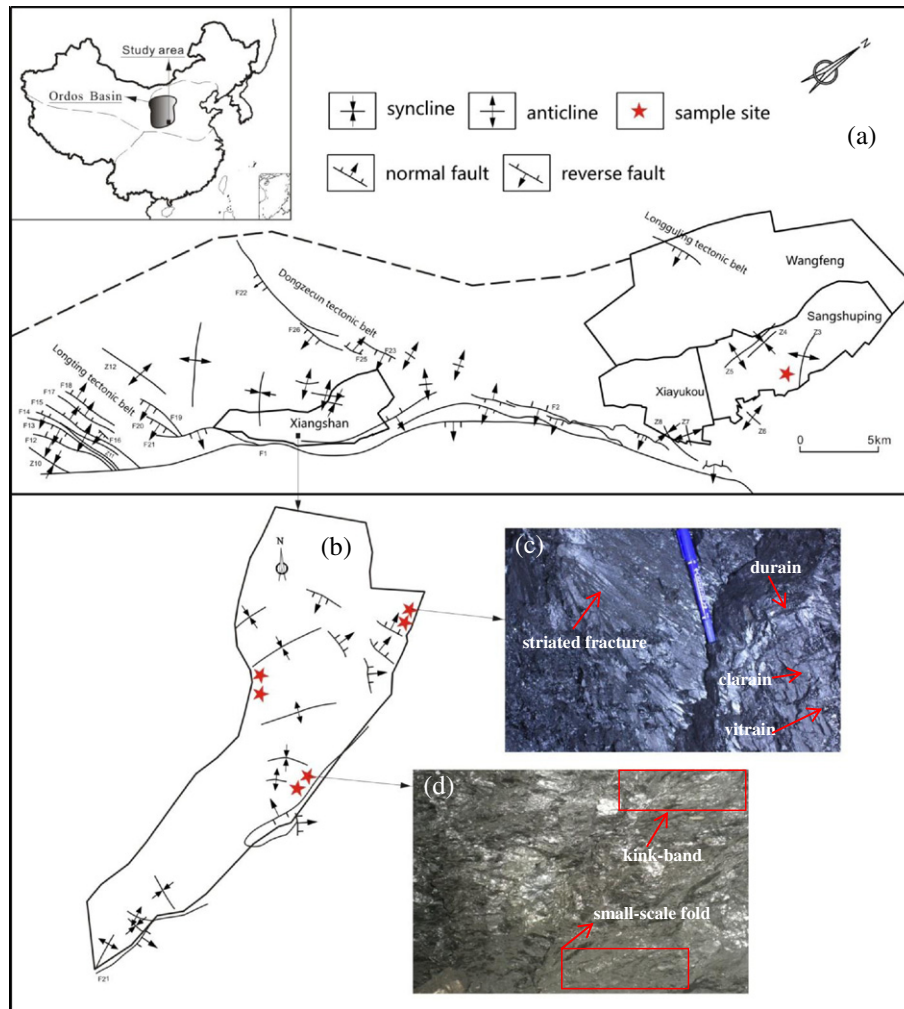
Fig. 1. The schematic structural map and the sampling site in Hancheng mining district, southeastern margin Ordos Basin. (a) Regional structures and the location of coalmine; (b) structural map of Xiangshan coalmine; (c) tectonically striated fracture and preserved coal primary structure (e.g. bedding structure) indicating weak shear deformation. The pencil is 14.5 cm in length; (d) photograph showing polished coal deformation structure including small fold and kink band in shear zone. The stick is 5 cm in length.

coal samples in XS lie in these shear zone (Fig. 1b). Additionally, in underground mines, a different degree of tectonic deformation occurs in coal seam due to the uneven distribution of the structure. For example, within the XS coalmine, as shown in Fig. 1d, the coal seam called "soft-coal" band exhibits a change in overall structure and is extensively polished under intensive shear deformation. The small-scale structure, such as small fold and kink band, can be observed. In contrast, under weak shear deformation, coal lithotype and cleat can be distinguished as presented in Fig. 1c. Moreover, tectonically striated fracture (described in later Section 4.1) on coal surface can be found.

The coal-bearing stratum is mainly composed of Pennsylvanian Taiyuan Formation and Permian Shanxi Formation with a total thickness of 85–175 m and eleven coal seams. The main seams in the Taiyuan Formation are No. 5 and No. 11 and No. 3 is the main seam in the Shanxi Formation. The thicknesses of No. 3, No. 5 and No. 11 are 0–3 m, 0–10 m and 2–6 m, respectively. All the seven typical TDC samples were collected from No. 11 coal seam and were originally in the form of hand specimens taken from the active working faces. The deformation features of the experimental samples will be elaborated later.

3. Coal samples and experiments

The maximum vitrinite reflectance ($R_{o,max}$) measurements of the seven samples were performed following the GB/T 6948-2008 standard. These samples are low volatile bituminous coals with $R_{o,max}$ ranging from 1.720% to 1.857% (Table 1). Vitrinite contents of coals are from 19.5% to 83.7% and inertinite contents vary from 15.7% to 79.5%. Mineral matters vary between 0.4% and 2.6% (Table 1). The coal samples can be divided into vitrinite-rich coals and inertinite-rich coals using the arbitrary boundary of <50% vitrinite, respectively (Unsworth et al., 1989). That is, in addition to sample SSP16 defined as inertinite-rich coals, the rest of the samples are vitrinite-rich coals. The ultimate analysis and proximate analysis of the seven samples were carried out following methods GB/T 476-2008 and GB/T 212-2008, respectively. Results including ash and moisture contents, and carbon and hydrogen contents were given in Table 1.

Mercury injection porosimetry (MIP) analysis was performed using an Autopore 9310 Instrument (Micromeritics, America) from China University of Mining and Technology. The samples for MIP experiments were about a 2 g weight with a block size of 1–2 cm. Prior to each experiment, all the coal samples were dried at 60 °C for 12 h. The dry samples were evacuated from the low-pressure port to <50 μ mm Hg to remove the residual gas and moisture in the sample. To evaluate the pore diameter using the Washburn equation (Washburn, 1921), the contact angle between mercury and the pore surface of 130°, and the surface tension of 485 dyn/cm were used as suggested by Gan et al. (1972) and Gökhan Şenel et al. (2001). The measurements run up to a pressure of 206.75 MPa, indicating that pore diameter as small as 6 nm can be penetrated. In order to diminish the effects of microfracture and interparticle porosity at low mercury pressure, the pore size data of 10 μm

Table 1
Deformed feature, petrologic, and chemical analysis of selected coal samples.

Sample ID	Deformed feature	$R_{o,max}$ (%)	Maceral and mineral (%)			Proximate analysis (%, ad)		Ultimate analysis (%, dry)	
			Vitrinite	Inertinite	Mineral	Moisture	Ash yield	Carbon	Hydrogen
XS7	Cataclastic	1.857	53.2	44.8	2.0	1.06	6.22	85.61	3.66
XS1	Cataclastic	1.720	80.9	18.2	0.9	0.66	13.97	74.35	3.11
XS9	Cataclastic	1.777	83.7	15.7	0.6	0.70	12.82	76.66	3.41
XS5	Granulated	1.743	73.6	26.0	0.4	0.84	20.40	67.38	2.96
XS6	Granulated	1.838	61.1	36.9	2.0	1.20	7.26	82.81	4.73
XS8	Mylonitic	1.813	69.8	29.2	1.0	0.68	13.52	76.16	3.50
SSP16	Mylonitic	1.797	19.5	79.5	1.0	0.89	11.19	79.71	3.53

(0.12 MPa) was used as the upper limit according to the work of Unsworth et al (1989).

Scanning electron microscope (SEM) analysis on coal samples was carried out using Quanta-200F field emission electron microscope scanning at China University of Petroleum in Beijing. The SEM technique used in this study enables us to observe the coal microscopic deformation structure and to investigate morphology and sizes of pores and microfractures falling into macropore range (mainly >0.1 μm). In order to well analyze the microstructure of different TDCs, for each sample, three patches with a block size of 1 cm³ in different positions were chosen and the relatively flat coal surface of each sample was selected for SEM observation. For the examination, the selected samples were posted on the sample stage, and the attachment on the samples surface was cleaned using ear washing bulb, then the sample surfaces were sputter-coated with gold-palladium for SEM investigation.

True densities of the samples were measured by helium displacement using a Quantachrome UltraPyc 1000 helium pycnometer. N₂ adsorption at 77 K and CO₂ adsorption at 273 K were conducted using an automatic gas adsorption apparatus (NOVA-4200e, Quantachrome) to obtain pore volume in the pore size range of 2 nm to 200 nm and super-micropore (<2 nm) volume, respectively. Prior to the measurement, the sample was dried at 105 °C overnight in a vacuum oven. For both N₂ adsorption and CO₂ adsorption techniques, sample outgas time was 12 h and the operation temperature was 105 °C. The N₂ adsorption data were interpreted using Barrett–Joyner–Halenda (BJH) analysis for micropore volume, transition pore volume and some mesopore volume according to the desorption branch of the isotherm. The N₂ adsorption test for each sample was repeated twice, and the co-efficients of variation (CV) for BJH pore volume measurements were less than 3%. The CO₂ adsorption for super-micropore determination of each sample was also performed twice, and the CV of CO₂ adsorption amount were less than 1%. The super-micropore volume was obtained from the Dubinin–Radushkevich (DR) equation on the basis of CO₂ sorption isotherm. Typical results from the above measurements were shown in Table 2. In this study, in combination with MIP data and N₂ adsorption and CO₂ adsorption data, we can evaluate the coal compressibility and adjust the Hg pore volume, and then the PSDs

related to coal deformation structures after Hg data correction are further discussed. It is complicated to combine pore information from the three techniques due to different assumptions of pore models and experimental artifacts specific to each method. In spite of these difficulties, it is an effective method to gain insight into the distribution of pore sizes ranged from <2 nm to >10,000 nm in coals (Clarkson and Bustin, 1999; Gan et al., 1972; Unsworth et al., 1989).

4. Analysis

4.1. Mercury porosimetry analysis

Some previous studies found that coal compressibility has an obvious effect on MIP results when pressure exceeds 10 MPa (Friesen and Mikula, 1987). So, we calculated coal compressibility of the studied samples with pressure over 10 MPa. Coal compressibility can be defined as (Li et al., 1999):

$$k_c = \frac{dV_c}{V_c dP} \tag{1}$$

where dV_c/dP represents the coal matrix volume change as a function of pressure, and V_c is the coal matrix volume. Since coals contain a large amount of mesopores and micropores, some of the pores could not be penetrated by mercury even at the highest pressure applied, and V_c in Eq. (1) comprises some unfilled pores (Friesen and Mikula, 1988; Li et al., 1999).

For a compressible solid (Li et al., 1999):

$$\Delta V_{obs} = \Delta V_p + \Delta V_c \tag{2}$$

where ΔV_{obs}, ΔV_p and ΔV_c are the changes of observed mercury volume, pore-filling volume, and coal matrix compression volume, respectively.

A good linear relation can be observed in the plots of the observed mercury intrusion volume versus pressure with $P > 10$ MPa for different TDCs (Fig. 2a). A similar phenomenon also can be found in the work of Toda and Toyoda (1972) and Guo et al (2014). Therefore, $\Delta V_{obs}/\Delta P$

Table 2
Parameters obtained from MIP, N₂ and CO₂ adsorption analysis and true densities.

Sample ID	ρ_{He} g/cm³	$k_c \times 10^{-10}$ m²/N	Pore diameters from Hg injection					Pore diameters from N₂ adsorption				Pore diameters from CO₂ adsorption		
			V_{MIP} cm³/g	V_{MIP}^* cm³/g	$V_{micro-frac}$ cm³/g	V_{macro} cm³/g	V_{meso} cm³/g	S_{BET} m²/g	V_{BJH} cm³/g	V_{trans} cm³/g	V_{micro} cm³/g	S_{DR} m²/g	$V_{super-micro}$ cm³/g	$V_{ads-super}$ cm³/g
XS7	1.507	0.626	0.0236	0.0142	0.0037	0.0037	0.0030	0.676	0.0030	0.0018	0.0005	219.319	0.073	13.425
XS1	1.505	0.715	0.0281	0.0175	0.0040	0.0037	0.0038	0.737	0.0050	0.0025	0.0015	179.131	0.060	12.630
XS9	1.496	0.747	0.0322	0.0211	0.0069	0.0044	0.0033	0.927	0.0053	0.0029	0.0012	179.989	0.061	13.025
XS5	1.514	0.873	0.1053	0.0926	0.0105	0.0272	0.0477	0.868	0.0059	0.0018	0.0011	160.954	0.054	11.817
XS6	1.476	0.725	0.0877	0.0768	0.0079	0.0290	0.0330	0.727	0.0050	0.0027	0.0009	169.357	0.056	12.383
XS8	1.489	0.934	0.0895	0.0758	0.0095	0.0185	0.0411	0.742	0.0051	0.0028	0.0007	158.950	0.053	12.815
SSP16	1.559	0.886	0.0796	0.0672	0.0107	0.0189	0.0311	0.964	0.0025	0.0014	0.0004	146.528	0.049	9.800

V_{MIP}, original maximum mercury pore volume obtained from MIP; V_{MIP}^*, maximum mercury pore volume with compressibility correction; $V_{micro-frac}$, microfracture volume determined from mercury intrusion (>10,000 nm in diameter); V_{macro}, corrected macropore volume (1000–10,000 nm in diameter); V_{meso}, corrected mesopore volume (100–1000 nm in diameter); S_{BET}, BET specific surface area; V_{BJH}, the BJH total pore volume; V_{trans}, transition pore volume (10–100 nm in diameter) of BJH pore volume; V_{micro}, micropore volume (2–10 nm in diameter) of BJH pore volume; S_{DR}, Dubinin–Radushkevich (DR) specific surface area; $V_{super-micro}$, super-micropore volume (<2 nm in diameter); $V_{ads-super}$, volume of adsorbed amount in super-micropore.

can be assumed to be constant β under $P > 10$ MPa, that is, $\Delta V_c/\Delta P$ can be obtained approximately by (Li et al., 1999):

$$\frac{\Delta V_c}{\Delta P} = \beta - \frac{\sum\limits_{6nm}^{100nm} \Delta V_p}{\Delta P} \qquad (3)$$

where the sum of the volume of pores of 6–100 nm (equivalent pressure varies from 206.75 MPa to 10.99 MPa) can be obtained from N_2 adsorption data (Table 3). Constant $\Delta V_{obs}/\Delta P$ or $\Delta V_c/\Delta P$ is valid only if the pores included in the sample remain unchanged during compression (Li et al., 1999). Assuming $\Delta V_c/\Delta P$ is independent on pressure, and replacing dV_c/dP by $\Delta V_c/\Delta P$, the compressibility of the seven coal samples can be obtained by Eq. (1). Since the minimum pore size probed is limited by the highest pressure available with mercury instrument, it is reasonable that the true solid volume and micropores are compressed simultaneously (Li et al., 1999). Thus, V_c was determined from the sample true density plus the micropores obtained from CO_2 adsorption, and the mesopores below 6 nm from N_2 adsorption (Li et al., 1999). In Table 2, compressibility values, k_c, ranging between 0.626 and 0.934×10^{-10} m²/N, are in agreement with the values reported in the literatures (Guo et al., 2014; Toda and Toyoda, 1972).

The detailed discussion about Hg pore volume calibration method can be found in Li et al. (1999). The original observed mercury intrusion data and the corrected mercury intrusion data with compressibility correction were presented in Fig. 2b. It can be seen that the differences between original and corrected data indicate that coal compressibility
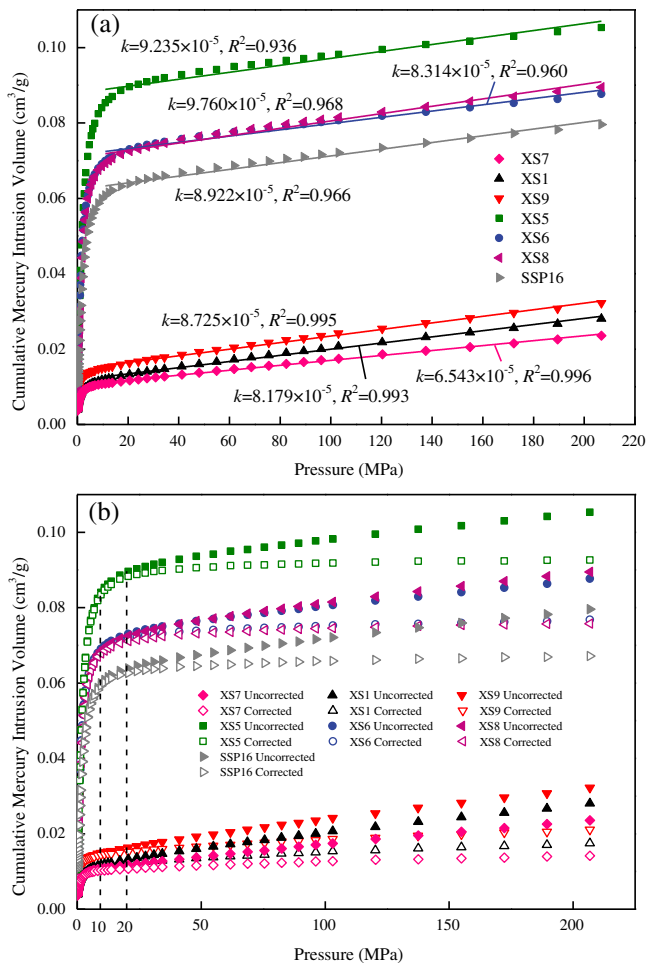
Table 3
Comparison of pore volume in the pore size range of 6–100 nm estimated by Hg injection and N_2 adsorption.

Sample ID	V (pore volume in the pore size range of 6–100 nm)		
	a	b	N_2
XS7	0.0116	0.0033	0.0020
XS1	0.0159	0.0054	0.0031
XS9	0.0169	0.0056	0.0034
XS5	0.0191	0.0084	0.0021
XS6	0.0170	0.0072	0.0031
XS8	0.0195	0.0068	0.0031
SSP16	0.0181	0.0066	0.0016

a, original mercury pore volume with pore size ranging from 6 nm to 100 nm; b, corrected mercury pore volume with pore size ranging from 6 nm to 100 nm.

has an obvious effect on Hg pore volume especially for pressure exceeding 20 MPa, which is compatible with the results obtained by Suuberg et al. (1995). Table 3 listed the pore volume in the pore size range of 6–100 nm where mercury intrusion and N_2 adsorption method overlap. As can be seen in Table 3, the difference in pore volume from the data of original MIP and N_2 adsorption on average accounts for 14.75% of total pore volume, while they are less than 5% from the data of corrected mercury and N_2 adsorption. The result coincides with that observed by Li et al. (1999). Taking into account of the effect due to coal compressibility, the corrected MIP data can generate multifractal parameters.

4.2. Multifractal analysis of Hg PSDs of coals

The multifractal analysis of PSDs can be performed through two-dimensional image analysis at a plane (Posadas et al., 2003) or by one-dimensional Hg injection at a size interval (Paz Ferreiro and Vidal Vázquez, 2010). Vidal Vázquez et al. (2008) have applied multifractal approach to assess one-dimensional PSDs estimated by Hg injection in soil. So, in our study, the multifractal analysis of one-dimensional Hg PSDs with pore volume–size data in coals is performed based on the work of Vidal Vázquez et al. (2008). The heterogeneity of PSDs can be characterized by the singularity spectrum or equivalently by the generalized dimensions using multifractal approach (Caniego et al., 2001; Muller and McCauley, 1992). However, the generalized dimensions have an easier handling and interpretation than singularity spectrum as suggested by Muller (1996) and Caniego et al. (2003). Thus, we use the generalized dimensions to assess the variability and heterogeneity of Hg PSDs.

To execute multifractal analysis of Hg PSDs for porous media supported on an interval $I = [a, b]$, a set of different boxes or subintervals of I with equal length ε is required (Vidal Vázquez et al., 2008). Mostly, the dyadic scaling down is widely used to partition the support I into a number of boxes $N(\varepsilon) = 2^k$ of box size, $\varepsilon = L \times 2^{-k}$ in k stages ($k = 0, 1, 2, 3...$), where L is the length of the interval I of pore size (Caniego et al., 2003). In these boxes or subintervals, the respective measures $p_i(\varepsilon)$ can be calculated from the available data.

In our case, the interval I of pore size that varied from 0.006 μm to 10 μm including 56 subintervals $I_i = [a_i, a_{i+1}]$ has been considered. The measure $p_i(\varepsilon)$ in each subinterval is the relative Hg pore volume data, V_i. In other words, the Hg pore volume data, v_i, are normalized, $V_i = v_i/\sum_{i=1}^{56} v_i$ ($i = 1, 2, 3..., 56$), with $\sum_{i=1}^{56} V_i = 1$.

Implementation of multifractal scaling for PSDs in the interval I of pore sizes requires dyadic partitions of I into boxes or subintervals of equal length (Montero and Martín, 2003). Thus, a rescaling of interval I of pore sizes is necessary. The most common way is logarithmic transformation. Under the transformation, the normalized pore size changes to $A_i = \log(a_i/a_1)$ ($i = 1, 2, 3..., 56$), and a new dimensionless interval $J = [0, 3.18]$ with subinterval of equal length, $J_i = [A_i, A_{i+1}]$ ($i = 1, 2, 3..., 56$) is obtained. Then a number $N(\varepsilon) = 2^k$ of boxes or subintervals of equal size $\varepsilon = L \times 2^{-k}$ for $k = 0$ to 5 will be then consecutively

Fig. 2. Plots of Hg pore volume for each gram of sample material as a function of pressure. (a) Linear regression of Hg pore volume versus pressure with $P > 10$ MPa using original MIP data; (b) comparison of Hg pore volume before and after correction.

generated in the normalized interval J of pore sizes. In order to ensure that each box has some concentration of pore volume, the maximum value for k is designated as 5 in this study. For any box or subinterval $J_i = [A_i, B_i]$, the measure $p_i(\varepsilon)$ can be obtained by adding all concentrations V_i with normalized pore sizes less than B_i and greater than A_i.

The probability density distribution of $\{p_i\}$ related to Hg porosity is then analyzed by the partition function, $\chi(q, \varepsilon)$ (Chhabra et al., 1989), which can be calculated from pore volume–size statistics by using

$$\chi(q, \varepsilon) = \sum_{i=1}^{N(\varepsilon)} p_i^q(\varepsilon) \tag{4}$$

where the moment order q is a real number, varying from $-\infty$ to $+\infty$. It serves as a "microscope" for exploring different regions of the pore volume–size distributions. For $q \ll 1$, the value of $\chi(q, \varepsilon)$ is largely determined by small $p_i(\varepsilon)$ data. For $q \gg 1$, the large $p_i(\varepsilon)$ data contribute most to $\chi(q, \varepsilon)$. Thus the variation of $\chi(q, \varepsilon)$ with different q splits the measure into subsets dominated by locally high or small concentration of porosity. Then, the distribution of local porosity can be represented by a series of generalized dimensions, D_q, (Muller, 1996), defined by Grassberger and Procaccia (1983), based on the work of Rényi (1955) for all $D_q \neq 1$, as follows:

$$D_q = \lim_{\varepsilon \to 0} \frac{1}{q-1} \frac{\log[\chi(q, \varepsilon)]}{\log(\varepsilon)} = \lim_{\varepsilon \to 0} \frac{1}{q-1} \frac{\log\left[\sum_{i=1}^{N(\varepsilon)} p_i^q(\varepsilon)\right]}{\log(\varepsilon)} \tag{5}$$

For $q > 0$, D_q emphasizes areas with a high concentration of porosity. For $q < 0$, D_q amplifies areas of low concentration (Caniego et al., 2003; Muller, 1996). For $q = 1$, Eq. (5) is uncertain. In this case, D_1 is evaluated by L'Hôpital rule:

$$D_1 = \lim_{\varepsilon \to 0} \frac{\sum_{i=1}^{N(\varepsilon)} p_i(1, \varepsilon) \log[p_i(1, \varepsilon)]}{\log(\varepsilon)} \tag{6}$$

Then, the set of points (q, D_q) generates a curve that describes the Rényi or D_q spectrum of the measure p_i. The D_q value at $q = 0$, $q = 1$ and $q = 2$ corresponds to the capacity dimension D_0, information dimension D_1, correlation dimension D_2, respectively. It is noted that for one-dimensional distribution, the value of $D_0 = 1$ when all the sub-intervals contain some pore volume data (San José Martínez et al., 2010). As proposed by Riedi et al. (1999), the correlation dimension D_2 also can be written as

$$D_2 = 2H - 1 \tag{7}$$

where H is called the Hurst exponent, varying from 0.5 to 1, usually associated with positive autocorrelation or long-range spatial variation (Feder, 1988). Then the autocorrelation in long-range spatial variations of porosity along the pore size intervals can be parameterized by the Hurst exponent (San José Martínez et al., 2010). In the case of monofractal distribution, the D_q spectrum is a horizontal line, i.e., $D_0 = D_1 = D_2$. For a multifractal structure, this spectrum is a monotone decreasing function of q with a sigmoidal shape and the values of D_0, D_1, and D_2 ranks as $D_0 > D_1 > D_2$ (Caniego et al., 2003).

5. Results and discussions

5.1. Structural characterization

Based on hand specimen examination and SEM observation, the degree of tectonic deformation is evaluated by the destruction of coal primary structure (e.g. banded structure of maceral composition), particle size and hardgrove grindability index (HGI) of coal, fracture properties and strain markers of deformation structure.

The sample XS7 is dominated by bright lithotype with developed lineation structure of clarain and conchoidal fracture. Irregular reticular fractures occur (Fig. 3a), indicating weak brittle failure (Su et al., 2001). "Feather-like" or radial fractures with dull lustre occur on coal surface (Fig. 3b). A similar phenomenon also can be found in the work of Bustin (1982a) and Frodsham and Gayer (1999). They suggested that these "feather-like" fractures may be the result of static and brittle shear failure and they defined it as striated fracture. The coal can be easily split into 2–5 mm-scale particles along the reticular fracture and the HGI is 61. SEM observation shows that the coal displays plate-like or wedge-shaped angular structure due to shearing fracture (Fig. 4a) or tensional fracture (aperture varies from 1–6 μm) (Fig. 4b) and micro-scale interlayer-sliding by fracture with aperture of 3.39 μm (Fig. 4b). The interconnected layer-fracture and cleat (non-tectonic fracture) are favorable for gas flow (Fig. 4c). Micro-scale thrust occurs along a bedding shear zone (Fig. 4c). Angular fragments of coal define the sense of shear as sinistral (Fig. 4d). The bright conchoidal fracture and dull tectonically striated fracture are observed by means of SEM observation (Fig. 4e).

The macrolithotype of sample XS1 is mainly semibright with little banded dull. The bedding structure is obvious. The coal is cut by oblique tectonic-fracture and is easily split along these fractures (Fig. 3c). The coal is relatively hard and the HGI is 47. Under SEM, block structure with displacement between blocks occurs along the tectonic fracture (Fig. 4f). The mineral band structure is well preserved (Fig. 4f). The coal is composed of different sized breccias by shearing fracture and tensional fracture which can be filled by pyrite (Fig. 4g). The conchoidal fracture is well developed on coal surface (Fig. 4g). The elongate pores in inertinite-rich layer between vitrinite-rich layer are formed under brittle compression (Fig. 4h).

The macrolithotype of sample XS9 is dominated by semibright and the fracture is mainly tectonic-fracture. Massive small fractures in different directions divide the coal into subangular or lumpy particles with size of approximately 1 cm. Large-scale irregular friction mirror surfaces can be observed (Fig. 3d). The HGI of this coal is 52. Under SEM, the fracture surface is occupied by parallel ridges and grooves (Fig. 4i). The coal shows parallel angular structure by shearing fracture or cleavage (Fig. 4j).

Sample XS5 has porphyritic texture with dull lustre. The macrolithotype of porphyritic angular blocks with multidirectional small-scale tectonic fracture is dominated by semibright (Fig. 3e). Irregular friction mirror surfaces with reticular fracture occur along the slip plane (Fig. 3f). The coal is easy to crumble into mm-scale grains and the HGI is 85. Microscopically, the coal is composed of fragments of coal clasts without internal deformation and the size of clasts is mainly less than 20 μm (Fig. 4k). Microfracture and inter-granular pores with aperture mainly less than 5 μm are formed between these coal clasts (Fig. 4l). Polished fractures associated with a thin layer of granular coal beneath the fracture plane are pervasive (Fig. 4l, m), which lies in the observation of Frodsham and Gayer (1999), who suggested that these fractures are the product of dynamic and brittle shear failure. The open and zigzagged fracture with aperture of 5.12 μm (Fig. 4n) and striated fracture (Fig. 4o) also can be found in this coal.

Sample XS6 has similar deformation feature with sample XS5. The bedding structure and non-tectonic fracture are strongly damaged. The coal has lenticular texture with dull lustre (Fig. 3g). The coal is easy to crumble into mm-scale grains and the HGI is 93. SEM observation shows that the coal clasts (size can be less than 2 μm) are well developed (Fig. 4p). Fig. 4q shows that the inertinite is subjected to heterogeneous deformation. To the left is cracked inertinite, while slip plane and thin layers of coal clasts occur under shear stress on the right, showing a mortar texture.

Sample XS8 and Sample SSP16 have similar deformation structure. Both are characterized by mixed petrographic components with dull lustre and strongly wrinkled structure, indicating obvious ductile deformation (Fig. 3h, i) as suggested by Bustin (1982b) and Li (2001). The

Fig. 3. Photographs showing various tectonically deformed coals. (a) Cataclastic coal with clarain bands for sample XS7; (b) striated fracture with dull lustre for sample XS7; (c) cataclastic coal with bedding structure for sample XS1; (d) cataclastic coal with angular structure for sample XS9; (e) granulated coal for sample XS5; (f) granulated coal with irregular friction mirror surfaces for sample XS5; (g) lenticular texture with dull lustre of granulated coal for sample XS6; (h) and (i) mylonitic coal with wrinkled texture for samples XS8 and SSP16, respectively.

coal is highly friable and the HGI is 138 for XS8 and 118 for SSP16, respectively. The SEM observations of these two coals are summarized as follows. Kink band with micro-scale fold occurs in inertinite-rich layers (Fig. 4r) and vitrinite-rich layers (Fig. 4s). Ductile behavior of the coal is also identified by bookshelf sliding with sinistral shear (Fig. 4t) and S–C band structure with dextral shear (Fig. 4u). "Honeycomb-like" pores with size mainly less than 5 μm are formed between coal clasts (Fig. 4v). Polished fracture surface under shearing process is also recorded (Fig. 4w).

According to the particle size and microstructure properties analyzed above, samples XS7, XS1 and XS9 can be classified as cataclastic coal, samples XS5 and XS6 are divided into granulated coal, while samples XS8 and SSP16 can be assigned to mylonitic coal based on the work of Frodsham and Gayer (1999) and Li (2001). The results confirm that granulated coals and mylonitic coals have been subjected to more intensive deformation than cataclastic coals.

5.2. Pore size distributions of different TDCs

Table 2 presented the pore volume obtained from the corrected Hg injection data and the original N_2 and CO_2 data of TDCs. The PSDs determined from the corrected MIP data for coal samples were shown in Fig. 5. As can be seen in Fig. 5 and Table 2, all the cataclastic coals show multi-model distribution of pore sizes and the pore volume

with pore size larger than 30 nm in cataclastic coals varies from 0.0077 cm^3/g to 0.0094 cm^3/g, which falls into the range of macropore volume for vitrinite-coals in low volatile bituminous rank reported by Gan et al (1972) and Unsworth et al (1989), who adopted macropore size in the range of 30–2960 nm and 30–10,000 nm, respectively. The macro- and mesoporosity in cataclastic coals are low (8.14% to 10.56%), but super-micropore approximately accounts for 85.55% of the total porosity (seen in Table 2), which may be caused by maceral composition.

In comparison to cataclastic coals, the macro- and mesopore volumes of granulated and mylonitic coals sharply increase, and the greatest amount of pore volume in the pore size range of 300–1000 nm (corresponding pressure ranges from 1.2–0.6 MPa) with the highest frequency of pores at diameter about 740 nm is noticed (Fig. 5). The results indicate that granulated and mylonitic coals possess six to nine times seepage–pore volume (macro- and mesopore volume) than cataclastic coals, which is consistent with the findings of Li et al. (2003), who applied mercury injection to characterize pore structure of TDCs. However, the super-micropore volume, DR surface area and super-micropore sorption capacity of granulated and mylonitic coals are smaller than those of cataclastic coals, and the adsorption pore volume and surface area of vitrinite-rich coals are higher than those of inertinite-rich coals (Table 2). Moreover, it is found from Fig. 2b that the slopes of volume-pressure curves for granulated and mylonitic

Fig. 4. Microscopic deformation structures of the test coal samples under SEM (scale is μm). (a) Plate-like or wedge-shaped angular structure under shearing fracture; (b) micro-scale interlayer-sliding by tensional fracture; (c) interconnected layer-fracture and cleat and micro-scale thrust, indicating brittle failure; (d) angular fragments of coal, indicating a sinistral sense of shear; (e) tectonically striated fracture with dull lustre; (f) block structure with displacement between blocks and mineral band structure; (g) tectonic fracture and conchoidal fracture; (h) elongate pores in inertinite-rich layer; (i) polished fracture surface with parallel ridges and grooves; (j) angular structure under shearing fracture; (k) fragments of coal clasts without internal deformation; (l) microfracture and inter-granular pores between clasts; (m) polished fractures associated with a thin layer of granular coal beneath the fracture plane; (n) open and zigzagged fracture; (o) striated fracture; (p) fragments of coal clasts; (q) polished fracture and thin layer of granular coal in inertinite component; (r) kink band with micro-scale fold in inertinite component of SSP16; (s) kink band with micro-scale fold in vitrinite component and foliated structure of XS8; (t) bookshelf sliding with sinistral shear of SSP16; (u) S–C band structure with dextral shear of XS8; (v) "honeycomb-like" pores between coal clasts of XS8; (w) polished fracture surface and coal clasts.

coals are nearly horizontal when pressure is far beyond 20 MPa (corresponding pore diameter smaller than 60 nm). These characteristics imply that the increasing tectonic deformation mainly leads to the enhancement of seepage–pore volume while have less contribution to

the variation in adsorption–pore volume, which was the case in the study of Qu et al (2010), who found that tectonic deformation mainly reforms the volume of bigger pores (pore size above 100 nm) obtained by MIP method.
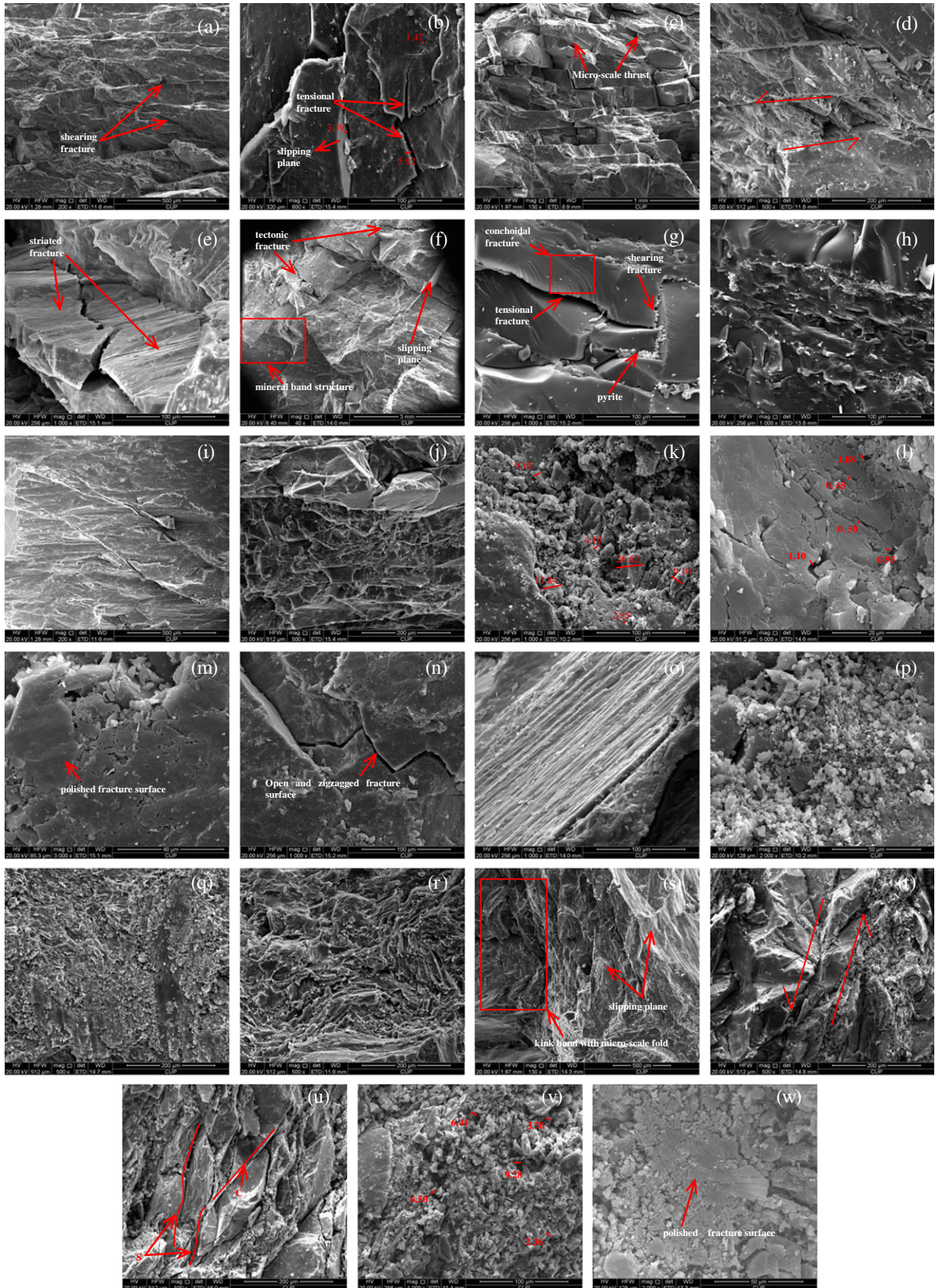
According to others' investigations (Adeboye and Bustin, 2013; Chalmers and Bustin, 2007; Mares et al., 2009), for the iso-rank coals, the maceral type is another important factor affecting pore volume and pore size distribution. Relationship of coal maceral content, macropore volume, mesopore volume, combined trans- and micropore volume and super-micropore volume in the test coal samples was presented in Fig. 6. It is observed that, for the coal samples studied, there is no correlation between the maceral type and macro- and mesopore volume (Fig. 6a and Fig. 6b). However, as shown in Fig. 6c, there is a positive correlation between combined trans- and micropore volume and vitrinite content ($R^2 = 0.975$) and conversely, a negative trend can be observed between combined trans- and micropore volume and inertinite content ($R^2 = 0.975$). The super-micropore volume increases with increasing vitrinite content and decreases with increasing inertinite content except sample XS7 (Fig. 6d). The sample XS7 has the highest super-micropore volume, DR specific surface and the highest adsorbed amount of CO_2 which possess a mixture of vitrinite and inertinite (Table 2). The results lie in the findings of Lamberson and Bustin (1993), who suggested that high semifusinite in some coals may create more super-micropore and sorption capacity than vitrinite. These results confirm that the complexity and variability of coal maceral within a narrow range of degree of coalification (1.720% to 1.857%) have predominant effect on the distribution of super-micropores (Clarkson and Bustin, 1996). Generally, vitrinite-rich coals have lower macroporosity, higher microporosity and greater sorption capacity than inertinite-rich coals within the iso-rank, which was the case in many studies (Giffin et al., 2013; Prinz et al., 2004).

The variation of pore volume and the relationship between pore volume and maceral composition indicate that tectonic deformation mainly contributes to seepage-porosity and weakens the effect of maceral composition on macro- and mesoporosity. Consequently, poor correlation occurs between maceral composition and macro-and mesoporosity. Similar results also can be found in the work of Li et al. (2003). However, maceral type mainly determines the distribution of adsorption-pores, while tectonic deformation has no or very little effect on the variation of adsorption-pores among the coals studied here. The increment of macro- and mesoporosity in granulated and mylonitic coals may be attributed to the presence of microfracture (aperture lower than 10 μm) and inter-granular pores formed during deformation process. The coal particles form tiny clasts under intensive shear deformation as depicted in granulated and mylonitic coals in Section 5.1. A dense cluster of microfracture and inter-granular pores with pore size mainly less than 5 μm form between these clasts (Fig. 4k, l, p, v, w), which corresponds to the increasing range of seepage-pores. Zhang (2001) also found that the size of inter-granular pore varies from 0.5 μm to 5 μm falling into the range of meso- and macropore sizes based on the observation of SEM, which confirmed our results. Therefore, the developed microfracture and inter-granular pores are responsible for the increase of seepage–pore volume under increasing tectonic deformation.

5.3. Multifractal analysis of Hg PSDs of different coals

The double log plots of partition functions, $\chi(q, \varepsilon)$, versus box size, ε, estimated from Eq. (4) are built for box size range ε $[L \times 2^{-k}, 1]$ ($0 \le k < 6$) and moment range q $[-10, 10]$. Fig. 7 presented two selected plots of $\log\chi(q, \varepsilon)$–$\log\varepsilon$ for Hg PSDs with the best (XS7) and the worst (XS6) linear correlation. If $\chi(q, \varepsilon)$ versus ε obeys a power law scaling or a linear relationship can be observed between $\log\chi(q, \varepsilon)$ and $\log\varepsilon$, the distribution of pore sizes in porous media is considered a multifractal distribution (Muller, 1996). All coal samples show a good linear relationship between $\log\chi(q, \varepsilon)$ and $\log\varepsilon$ with coefficients of determination, R^2, larger than 0.96 for all values of q (Fig. 7). This illustrates that the PSDs of coals have multifractal characteristics. Thus, it is necessary to explore the inner variations in PSDs of different coal samples.

Generalized dimensions, D_q, calculated from Eqs. (5) and (6) for different coals were listed in Table 4 and the D_q spectra were presented in Fig. 8. From Fig. 8, it is found that all the spectra follow a monotone decreasing function of q with a sigma-shaped curve. Moreover, from Table 4, the three dimensions for all samples follow the order as: $D_0 > D_1 > D_2$. The shape of the D_q spectra and the variation of D_q values reveal that the PSDs of coal samples have properties close to multifractal self-similarity measures, which is in good agreement with the observation from $\chi(q, \varepsilon)$ presented above.

The shape and parameters of D_q spectra including information dimension D_1, the Hurst exponent H, the width D_{-10}–D_{10} of D_q spectrum, the width of right side D_0–D_{10} of D_q spectrum and the width of left side D_{-10}–D_0 of D_q spectrum listed in Table 4 give information about the inner variability in the distribution of pore sizes and also depict the heterogeneity in size-dependent distribution of porosity (Paz Ferreiro and Vidal Vázquez, 2010). The wider the D_q spectrum, the higher is the complexity or heterogeneity in PSDs (Vidal Vázquez et al., 2008).

The narrowest D_q spectrum or the smallest value of D_{-10}–D_{10}, indicative of the lowest degree of heterogeneity in the distribution of porosity along the pore size intervals, can be observed in sample XS7 (Table 4). The widest distributions of D_q spectrum is found in sample XS6 (Table 4), indicating the highest degree of multifractality or inhomogeneity in PSDs. However, the D_{-10}–D_{10} values do not always grow with increasing tectonic deformation. For example, the value of D_{-10}–D_{10} of sample XS9 is almost close to XS5 but larger than sample XS8 (Table 4). This may be caused by the joint action of factors that affect the pore volume and size-distribution of pores. The variation of PSDs may be related to coal rank, maceral type, moisture, carbon and ash content and tectonic deformation (Clarkson and Bustin., 1996; Giffin et al., 2013; Hou et al., 2012; Li et al., 2003). Since the variation of width D_{-10}–D_{10} of D_q spectrum reflects the heterogeneity in the distribution of porosity over the whole pore size range, it may be the comprehensive result of these factors and cannot completely reflect the main distinction in PSDs for coals with different structure.

However, significant differences exist in the shape variation of D_q versus q. For cataclastic coals, the D_q spectra show a quasi-linear variation for $q > 0$, whereas a sigma-shaped curve for $q < 0$ even if it is not very obvious in sample XS7 (Fig. 8). On the contrary, the variations of D_q with respect to q exhibit a reverse trend in granulated and mylonitic coals. The D_q spectra of samples XS5, XS6, XS8 and SSP16 show a rather sigma-shaped curve for $q > 0$, while a quasi-linear variation D_q versus q for $q < 0$ is observed. These variations of D_q with respect to q also can be confirmed by the comparison of widths of left side D_{-10}–D_0 and right side D_0–D_{10} of D_q spectra (Table 4). From Table 4, in granulated and mylonitic coals, the D_0–D_{10} values are larger than the values of D_{-10}–D_0 and the difference is higher than 0.1, whereas negative trend can be observed in cataclastic coals.

The variation of the right part D_0–D_{10} for $q > 0$ and left part D_{-10}–D_0 for $q < 0$ of D_q spectra corresponds to dominance of large and small concentration of porosity, respectively (Caniego et al., 2003; Paz Ferreiro and Vidal Vázquez, 2010). Consequently, the change of multifractal parameters for $q > 0$ may be due to various distributions of pore size larger than 100 nm (seepage-pores) and parameters for $q < 0$ can be assigned to pore size smaller than 100 nm (adsorption-pores) as presented in Fig. 5. Quasi-linear shape stands for a homogeneous distribution of pore sizes, whereas sigma-shaped curve stands for a heterogeneous distribution of pore sizes (Caniego et al., 2003). Hence, cataclastic coals show a homogeneous structure in the inner distribution of seepage-pores but a heterogeneous structure in the inner distribution of adsorption-pores, while the opposite trend is noticed in granulated and mylonitic coals.

Additionally, granulated and mylonitic coals have more concave up shape for $q > 0$ and greater widths of right side D_0–D_{10} than cataclastic coals, which indicate that tectonic deformation increases the variability and heterogeneity in the inner distribution of seepage-pores. However, it is not a common phenomenon in the widths of left side D_{-10}–D_0 of D_q spectra ($q < 0$), as the values of D_{-10}–D_0 in some cataclastic coals are
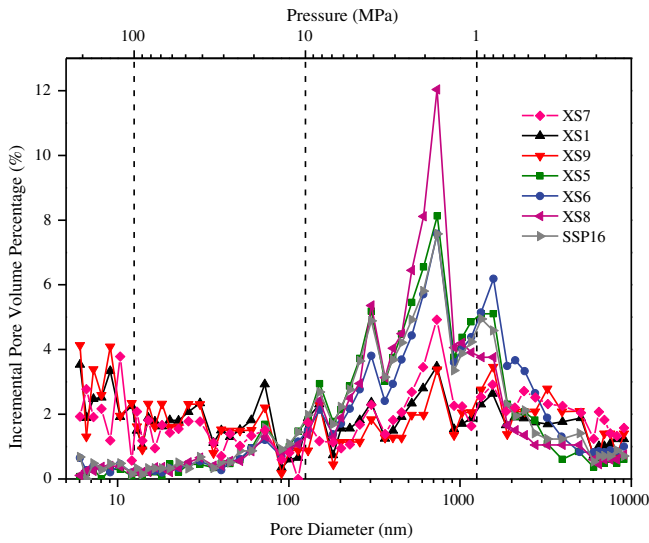
Fig. 5. Mercury pore size distribution of different tectonically deformed coals.

wider than those in granulated and mylonitic coals. For example, the sample XS9 characterized by the highest vitrinite content has the greatest D_{-10}–D_0 value, while the smallest D_{-10}–D_0 value occurs in sample SSP16 represented by the greatest inertinite content. This phenomenon indicates that the right branch of D_q spectra mainly reflects the influence of tectonic deformation on the PSDs of coals and maceral type exerts important effect on the variation of left side D_{-10}–D_0 of D_q

spectra. The above analysis is compatible with the results of PSDs in Section 5.2 that tectonic deformation and maceral composition exert primary control on the distribution of seepage-pores and adsorption-pores, respectively.

The capacity dimension, D_0, represents the scaling of non-empty boxes containing some porosity under successive finer partitions, which is independent of the probability of the porosity in each box (Caniego et al., 2003; Muller and McCauley, 1992). From Table 5, the values of D_0 are always 1.000 for all samples, which corresponds to the Euclidean dimension of one for one-dimensional distribution. This is probably due to the fact that, when all the boxes have some concentration of porosity, the partition function $\chi(0, \varepsilon)$ in Eq. (4) equals the total number of boxes $N(\varepsilon)$ covering the pore size length, so D_0 shown in

Eq. (5) can be expressed as $D_0 = \lim_{\varepsilon \to 0} \frac{\log N(\varepsilon)}{\log(\varepsilon)}$, which scales with

Euclidean exponent one. This result is consistent with the conclusion of other scholars (Paz Ferreiro and Vidal Vázquez, 2010; San José Martínez et al., 2010; Vidal Vázquez et al., 2008).

The information dimension, D_1, provides information about the concentration degree of distribution of porosity along pore size intervals (Vidal Vázquez et al., 2008). The maximum value of D_1 is D_0 which occurred in monofractal PSDs (Paz Ferreiro and Vidal Vázquez, 2010). The values of D_1 are closer to D_0, the porosity is more evenly distributed across the range of pore sizes. And conversely the smaller the values of D_1, the more clustered the pores, the higher the porosity is concentrated in a small domain of the study scale and the higher degree of heterogeneity occurs in inner PSDs (Caniego et al., 2003). Table 5 showed that the values of D_1 for cataclastic coals vary from 0.966 to 0.974, rather close to D_0, an indicator of a rather homogeneous distribution of
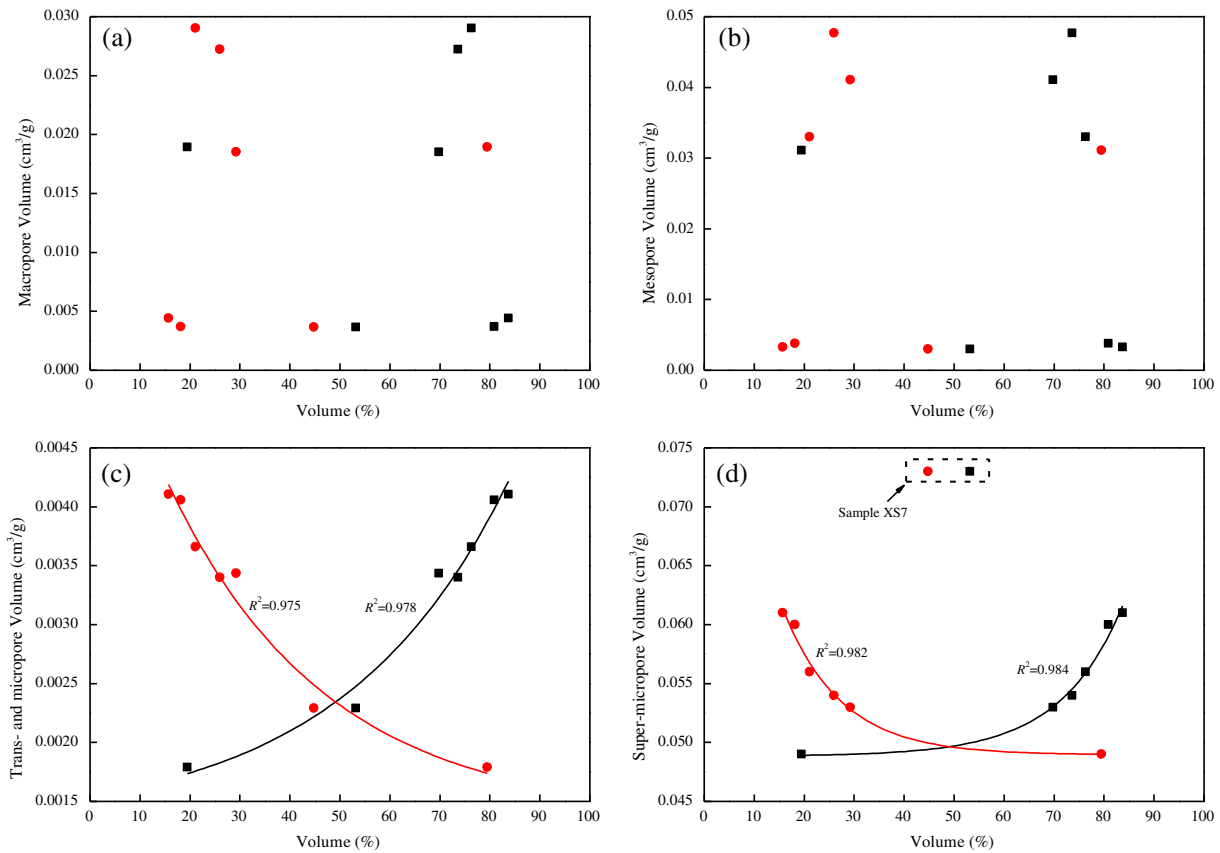

Fig. 6. Relationship of maceral composition and pore volume in coal samples. (a) Relationship between vitrinite, inertinite and macropore volume; (b) relationship between vitrinite, inertinite and mesopore volume; (c) relationship between vitrinite, inertinite and combined trans- and micropore volume; (d) relationship between vitrinite, inertinite and super-micropore volume. Vitrinite is black solid symbol and inertinite is red solid symbol.

porosity over the range of pore sizes. In contrast, the lower D_1 values (0.860 to 0.896) of granulated and mylonitic coals suggest increased clustering of PSDs, so that most of the porosity concentrates in a narrow range of equivalent diameter sizes and higher degree of unevenness of inner PSDs occurs. These results are compatible with a relatively regular multi-model PSDs of cataclastic coals in Fig. 5, which contrast with narrow and high fluctuant PSDs of granulated and mylonitic coals in Fig. 5. It is observed that the D_1 increases as the porosity in pore size above 100 nm increases due to increasing tectonic deformation. This implies that the increment in seepage-porosity, mainly in 1.0–0.3 μm pore diameter interval (Fig. 5), may be the main driver of the differences observed in D_1 values between coals with different structure. So, D_1 gives a good description of difference and variability in the inner size-distributions of seepage-pores of different coals.

The Hurst exponent, H, indicates the autocorrelation of distribution of porosity over the set of pore sizes related to long-range dependencies (San José Martínez et al., 2010). The value of H closer to 1 means that the stronger autocorrelation does exist in size-dependent distribution of porosity (San José Martínez et al., 2010). The mean values of H for cataclastic, granulated and mylonitic coal samples are 0.971, 0.873 and 0.893, respectively (Table 5). All the values of H for different coal samples are close to 1, indicating positive autocorrelation in the variation of porosity among different pore size intervals. Although all the values of H are close to 1, differences are still found in the values of H in different coals. The mean H values of cataclastic coals are significantly larger than those of granulated and mylonitic coals, indicative of a higher autocorrelation in size-dependent distribution of porosity of cataclastic coals. This phenomenon also shows that the lower pore connectivity along the interval of pore sizes occurs with increasing tectonic deformation. Thus, H can be considered as an important parameter for estimating the evolution of pore connectivity across the range of pore sizes after increased tectonic deformation.

Previous studies show that the conventional fractal dimension (CFD) is an effective parameter to describe the geometrical complexity of PSDs of coals (Mahamud et al., 2003; Yao et al., 2009a; Zou et al., 2013). Since both CFD and multifractal parameters can be used to characterize the heterogeneity of PSDs, a correlation may exist between them. Here we investigated the relationship between these parameters. Three main mathematical models for CFD related to Hg PSDs were proposed by Friesen and Mikula (1987), Neimark (1990) and Zhang et al. (2006). In this study, the Zhang's model was chosen to determine the fractal dimension D_z of PSDs due to its lower deviations and higher correlation coefficients (Zhang and Li, 1995). A detailed description of the procedure of fractal theories developed by Zhang and coworkers (2006) can be found in our previous research (Zheng et al., 2015) where the method was already employed.

Fig. 9 showed the plots of $\ln(W_n/r_n^2)$ versus $\ln(V_n^{1/3}/r_n)$ for the test coals. Each graph includes the average fractal dimension D_z for the full range of pores. As presented in Fig. 9, for the coal samples studied, no obvious difference exists in D_z of different TDCs with different maceral
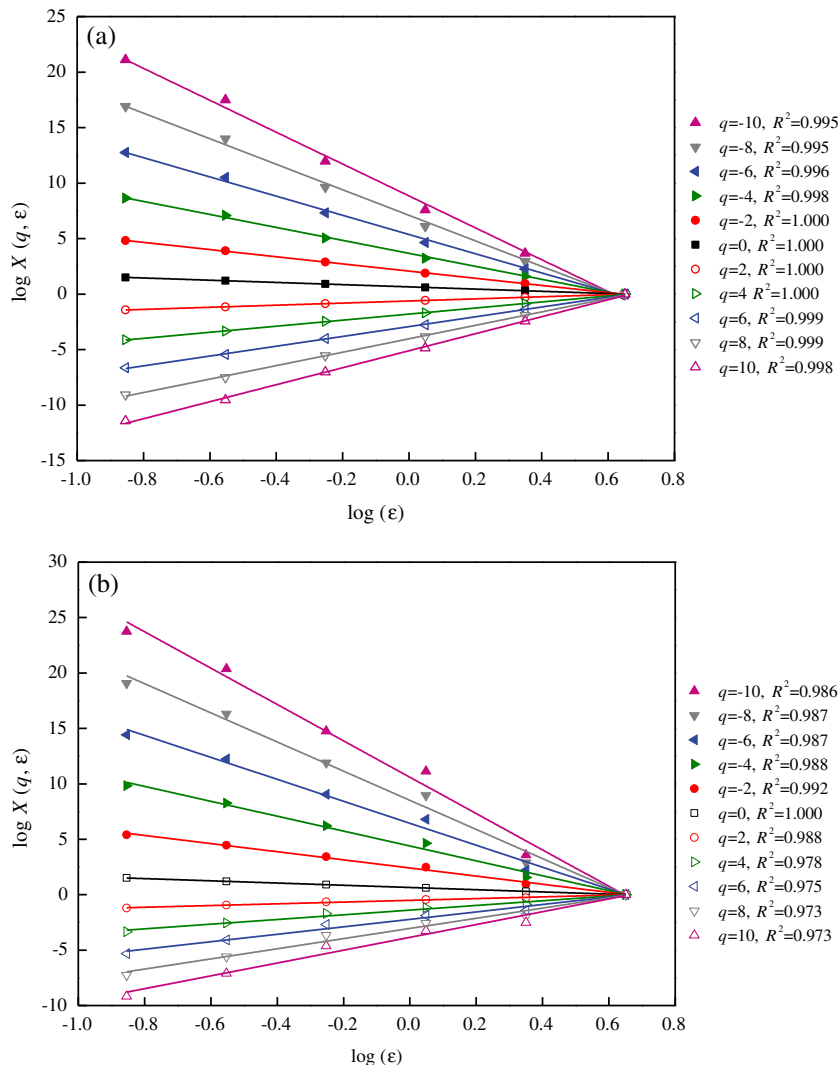

Fig. 7. Log plots of the partition function, $\chi(q, \varepsilon)$, versus box size, ε, for PSDs with the best (a. XS7) and the worst (b. XS6) linear correlation are shown.

Table 4
Selected multifractal parameters from the generalized dimension spectrum and conventional fractal dimensions for the test coal samples.

Sample ID	D_0	D_1	H	D_{10}	D_{-10}	D_{-10}–D_{10}	D_0–D_{10}	D_{-10}–D_0	D_{sp}	D_{ap}
XS7	1.000	0.974	0.977	0.899	1.202	0.303	0.101	0.202	2.694	2.713
XS1	1.000	0.964	0.968	0.837	1.320	0.483	0.163	0.320	2.669	2.995
XS9	1.000	0.966	0.967	0.793	1.393	0.600	0.207	0.393	2.701	2.999
XS5	1.000	0.885	0.891	0.625	1.230	0.604	0.375	0.230	2.802	2.402
XS6	1.000	0.860	0.871	0.566	1.300	0.734	0.434	0.300	2.757	2.427
XS8	1.000	0.890	0.901	0.652	1.216	0.564	0.348	0.216	2.805	2.406
SSP16	1.000	0.896	0.886	0.547	1.164	0.618	0.453	0.164	2.874	2.312

D_0 and D_1 are the capacity and information dimensions, respectively; H, the Hurst exponent; D_{10} and D_{-10} are the generalized dimensions for moment $q = 10$ and $q = -10$, respectively; D_{-10}–D_{10} is the width of D_q spectrum; D_0–D_{10} and D_{-10}–D_0 are the width of right side and left side of D_q spectrum, respectively; D_{sp} and D_{ap} are the conventional fractal dimensions corresponding to seepage-pore and adsorption-pore, respectively.

compositions. That is, the average fractal dimension D_z cannot discriminate between PSDs of TDCs. Under this situation, we calculated CFD D_{sp} and D_{ap} corresponding to seepage-pore and adsorption-pore respectively as suggested by the variations of D_0–D_{10} for $q > 0$ and D_{-10}–D_0 for $q < 0$ of D_q spectra. The results were shown in Table 4. It is observed that increasing tectonic deformation shows a trend to increase D_{sp}, while increasing vitrinite causes increasing D_{ap}. This is in line with the observation from D_0–D_{10} and D_{-10}–D_0 presented above. The results suggest that different pore size intervals show different self-similarities (multifractal scaling), so the average fractal dimension D_z over the whole pore size range is failed to characterize the variability of PSDs of coal samples with different deformation structures and petrographic compositions.

Linear regression analysis between CFD (D_{sp}, D_{ap}) and multifractal parameters was presented in Table 5. As shown in Table 5, D_{sp} is positively correlated with D_0–D_{10} and negatively correlated with D_1 and H. D_{ap} exhibits a positive trend with D_{-10}–D_0. The positive or negative correlation between D_{sp} or D_{ap} and multifractal parameters can be explained by the reason that these parameters reflect similar pore scaling properties dominating at different pore size intervals. However, multifractal analysis provides more parameters to quantitatively express the inner scaling behavior of PSDs of coal compared with conventional single fractal analysis. Since D_{sp} and the generalized dimension D_{-10}–D_0 characterize different scaling behavior of PSDs, the correlation between them is not analyzed, as well as D_{ap} and multifractal parameters for $q > 0$.

The above analysis suggests that scaling property or multifractality in PSDs of coals may depend on coal rank, maceral type, carbon content, ash content and tectonic deformation. The variation of multifractal scaling in Hg PSDs of coals with the same rank in our study may greatly

lie on tectonic deformation and maceral type. Therefore, the various factors, dominating at different pore size intervals, show specific influence on multifractal scaling in the distribution of pore sizes measured by Hg injection.

5.4. Relationship of porosity, maceral composition and multifractal parameters from Hg PSDs

Relationship of multifractal parameters, porosity (macro-, meso-, seepage- and combined trans- and microporosity) and maceral composition was performed through a linear regressive analysis (Table 5). The results show that macro-porosity and seepage-porosity are significantly and positively correlated to D_0–D_{10}, but negatively correlated to D_1 and H at the $p = 0.01$ level ($R > 0.85$). Mesoporosity shows similar correlation to above multifractal parameters for moment $q > 0$ at the $p = 0.01$ level with the exception of D_0–D_{10} (significant at the $p = 0.05$ level and $R = 0.814$). The macroporosity also positively correlates to D_{-10}–D_{10} at the $p = 0.1$ level, but the correlation coefficient is somewhat lower ($R = 0.666$). In contrast, combined trans- and microporosity show a positive correlation to multifractal parameter D_{-10}–D_0 for moment $q < 0$ at the $p = 0.05$ level, but exhibit lower correlation to multifractal parameters for $q > 0$ (R ranging from -0.389 to 0.436). The correlation between coal composition and multifractal parameters follows the similar tendency as combined trans- and microporosity. Vitrinite and inertinite shows a positively and negatively weak trend with D_{-10}–D_0 (significant at the $p = 0.1$ level) respectively but show no or little correlation to multifractal parameters for moment $q > 0$. It is worth noting that no clear correlation is found between moisture content, ash content, carbon content and multifractal parameters (data not shown). Thus, the effect of the aforementioned factors on multifractal scaling in Hg PSDs can be neglected.

The strong relationship between macro-, meso-, and seepage-porosity and multifractal parameters (e.g. D_1, H) for $q > 0$ can be interpreted as the fact that these parameters depict the heterogeneity and distribution of high concentrations of porosity (seepage-pore in our study) in Hg PSDs that are magnified by positive values of q. In contrast, the high correlation between trans-microporosity, maceral composition and multifractal parameter (D_{-10}–D_0) for $q < 0$ are
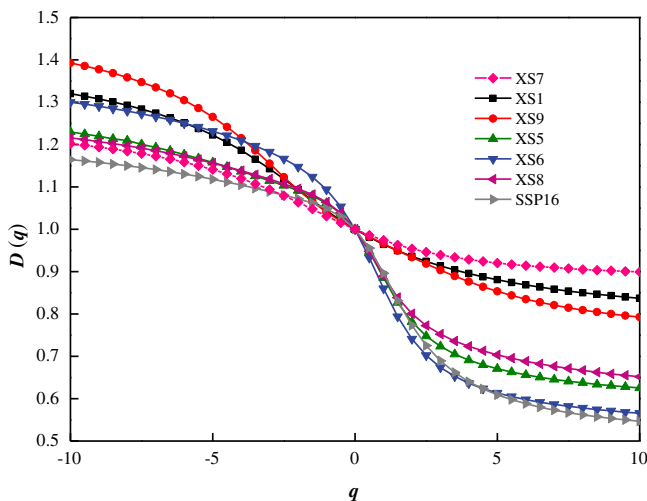
Fig. 8. Generalized dimension D_q, versus q from $q = -10$ to $q = +10$ for PSDs of the coal samples studied.

Table 5
Relationship of conventional fractal dimension D_{sp} and D_{ap}, porosity, maceral composition, and multifractal parameters from Hg PSDs.

	D_1	H	D_{-10}–D_{10}	D_0–D_{10}	D_{-10}–D_0
D_{sp}	$-0.688^\dagger$	-0.781^*	0.307	0.833^*	n
D_{ap}	n	n	nc	n	$0.687^\dagger$
Macroporosity	-0.972^{**}	-0.957^{**}	$0.666^\dagger$	0.877^{**}	-0.261
Mesoporosity	-0.901^{**}	-0.890^{**}	0.461	0.814^*	-0.292
Seepage-porosity	-0.949^{**}	-0.937^{**}	0.557	0.858^{**}	-0.177
Trans + microporosity	0.436	0.398	0.305	-0.389	0.824^*
Vitrinite	0.314	0.111	nc	-0.203	$0.685^\dagger$
Inertinite	-0.312	-0.094	nc	0.221	$-0.686^\dagger$

*, significant at the 0.05 probability (p) level; **, significant at the $p = 0.01$ level; †, significant at the $p = 0.1$ level; nc means no correlation is observed; n means not analyzed.
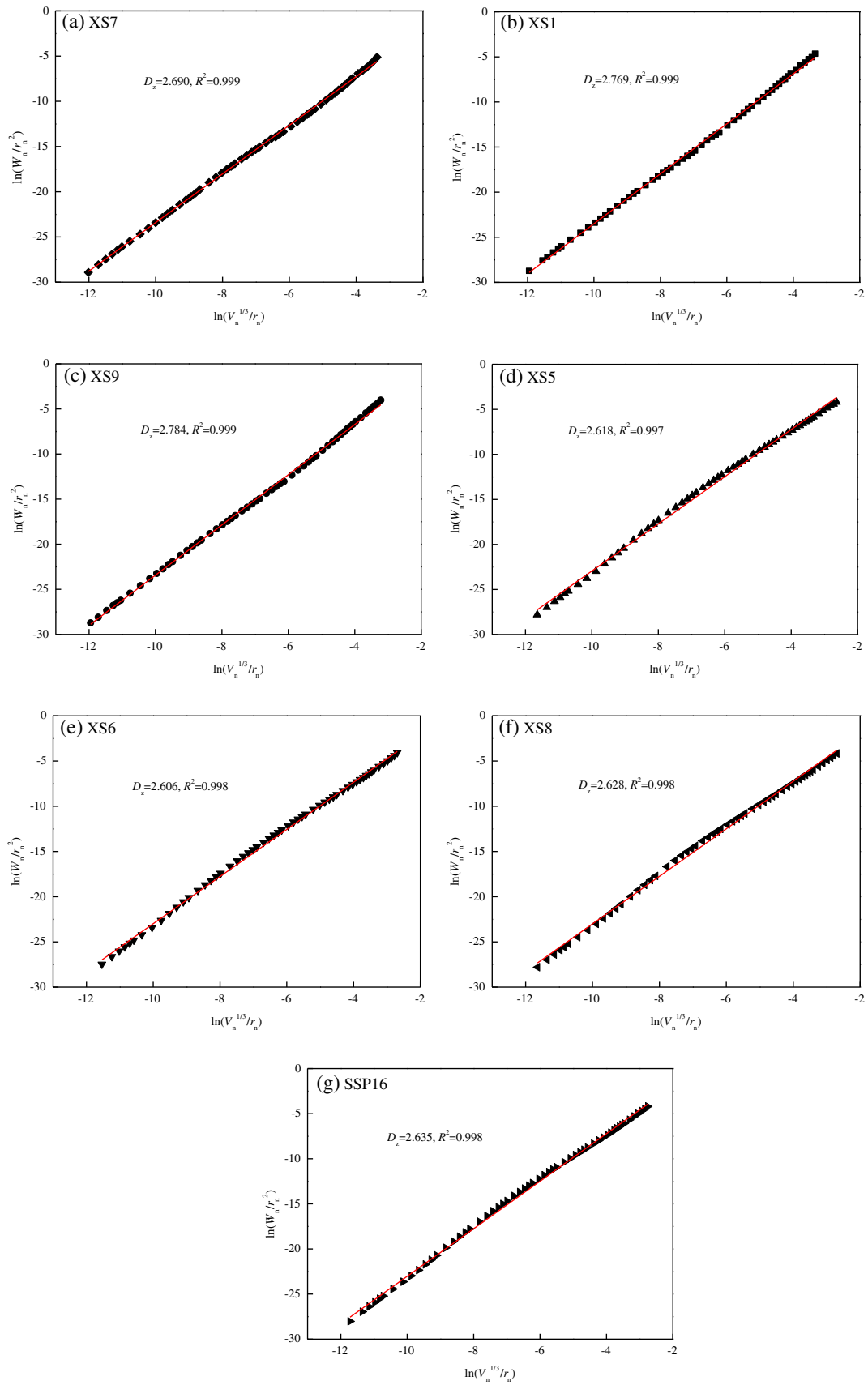
Fig. 9. Plots of $\ln(W_n/r_n^2)$ versus $\ln(V_n^{1/3}/r_n)$ for the test coal samples. The value of D_z is the average fractal dimension.

attributed to the parameter describing the variability and distribution of small concentrations of porosity (adsorption-pore in our study) in Hg PSDs that are magnified by negative values of q. However, there is little multifractal parameter to characterize the multifractal properties of adsorption-pores. Hence, it is necessary to fully characterize the size-dependent distribution of adsorption-porosity and the work focused on the multifractal analysis of PSDs based on nitrogen isotherms is currently being done to quantitatively explore how maceral type and other factors (e.g. ash content) affects the multifractality and important physical properties of inner size-distributions of adsorption-pores.

The above regression results suggest that, for the coals studied, the increasing macro- and mesoporosity or seepage-porosity caused by tectonic deformation induces higher clustering, lower autocorrelation, higher heterogeneity as estimated by generalized dimensions for $q > 0$. Therefore, the narrower distribution with higher fluctuation, lower pore connectivity and greater complexity in the inner distribution of seepage-pores occur in granulated and mylonitic coals when compared with cataclastic coals. The increasing seepage-porosity may relate to the presence of microfracture and inter-granular pores formed through deformation process as depicted in Section 5.2. Consequently, the uneven distribution of microfracture and inter-granular pores caused by tectonic deformation may be the main factors that affect the variation of generalized dimensions for $q > 0$ and induce a more heterogeneous distribution of seepage-porosity along the interval of pore sizes. Moreover, the strong correlation means that D_1, H and D_0–D_{10} can be treated as the predictive parameters that well discriminate between Hg PSDs of TDCs. However, the increment in combined trans- and microporosity due to increasing vitrinite leads to high heterogeneous distributions of adsorption-pores, which can be reflected by the positive relationship of trans-microporosity, maceral composition and multifractal parameter D_{-10}–D_0 for $q < 0$.

In summary, in comparison to single pore volume, this investigation shows that the multifractal parameters, such as D_1, H and D_0–D_{10}, can well describe the inner distribution of porosity along pore size intervals and distinguish the internal differences in Hg PSDs hidden in the pore volume–size data series for different coals in more detail. The multifractal analysis generates more useful parameters which can well elucidate how tectonic deformation affects the evolution and heterogeneity of Hg PSDs of coals.

6. Conclusions

In this work, in combination with mercury intrusion data and gas (N_2 and CO_2) adsorption data, the Hg pore volume under pressure > 10 MPa was corrected, and then the PSDs related to coal deformation structures after Hg data correction were investigated. The results show that, under the iso-rank conditions, tectonic deformation has a dramatic effect on seepage-porosity but has less contribution to the variation in adsorption-porosity for the coals studied. In contrast, the maceral type is the main control upon the distribution of adsorption-porosity especially for super-microporosity but has little contribution to the distribution of seepage-porosity due to the effect of tectonic deformation. Generally, seepage-porosity (macro- and mesoporosity) increases with increasing tectonic deformation, which may be attributed to the presence of microfractures and inter-granular pores formed during deformation process. Vitrinite-rich coals have greater amount of adsorption-porosity than inertinite-rich coals.

The shape of generalized spectra and the variation of generalized dimensions D_q with respect to q reveal that the PSDs of coal samples show multifractal behavior. Nevertheless, the extracted generalized dimensions from PSDs including information dimension D_1, the Hurst exponent H, the width of right side D_0–D_{10} of D_q spectra for moment $q > 0$ and the width of left side D_{-10}–D_0 of D_q spectra for moment $q < 0$ exist significantly difference in the coals studied. The variation of D_1, H, and D_0–D_{10} for $q > 0$ and a strong correlation between these parameters and seepage-porosity illustrate that tectonic deformation leads to

narrower distribution with higher fluctuation, lower pore connectivity and greater complexity in the inner distribution of seepage-pores. On the contrary, the D_{-10}–D_0 values for $q < 0$ and high correlation with adsorption-porosity suggest that increasing vitrinite content induces a heterogeneous structure in the inner distribution of adsorption-pores. Moreover, D_1, H, and D_0–D_{10} can well discriminate between PSDs of TDCs. Hence, multifractal approach is useful to characterize the internal heterogeneity and amplify the differences in PSDs of different coals.

A further step is needed to correlate such generalized dimensions to physical properties of TDCs, such as gas properties or permeability and mechanical properties or friability. Multifractal analysis may be a useful way to quantify these behaviors. Moreover, it is still need to further investigate how other factors, including coal rank and maceral composition, affect multifractal properties of distribution of adsorption-pores for coals.

References

Adeboye, O.O., Bustin, R.M., 2013. Variation of gas flow properties in coal with probe gas, composition and fabric: examples from western Canadian sedimentary basin. Int. J. Coal Geol. 108, 47–52.

Anovitz, L.M., Cole, D.R., Rother, G., Allard, L.F., Jackson, A.J., Littrell, K.C., 2013. Diagenetic changes in macro- to nano-scale porosity in the St. Peter Sandstone: an (ultra) small angle neutron scattering and backscattered electron imaging analysis. Geochim. Cosmochim. Acta 102, 280–305.

Bae, J.-S., Bhatia, S.K., Rudolph, V., Massarotto, P., 2009. Pore accessibility of methane and carbon dioxide in coals. Energy Fuel 23, 3319–3327.

Beamish, B.B., Crosdale, P.J., 1998. Instantaneous outbursts in underground coal mines: an overview and association with coal type. Int. J. Coal Geol. 35, 27–55.

Bustin, R.M., 1982a. Striated conical structures and related fractures in bituminous coal of the southern Canadian Rocky Mountains. Int. J. Coal Geol. 2, 1–16.

Bustin, R.M., 1982b. The effect of shearing on quality of some coals in the southeastern Canadian Cordillera. Can. Inst. Min. Metall. Bull. Am. Meteorol. Soc. 75, 76–83.

Bustin, R.M., Ross, J.V., Rouzaud, J.-N., 1995. Mechanisms of graphite formation from kerogen: experimental evidence. Int. J. Coal Geol. 28, 1–36.

Cai, Y.D., Liu, D.M., Pan, Z.J., Yao, Y.B., Li, J.Q., Qiu, Y.K., 2013. Pore structure and its impact on CH$_4$ adsorption capacity and flow capability of bituminous and subbituminous coals from Northeast China. Fuel 103, 258–268.

Caniego, F.J., Martín, M.A., San José, F., 2001. Singularity features of pore-size soil distribution: singularity strength analysis and entropy spectrum. Fractals 9, 305–316.

Caniego, F.J., Martín, M.A., San José, F., 2003. Rényi dimensions of soil pore size distribution. Geoderma 112, 205–216.

Cao, Y.X., Davis, A., Liu, R.X., Liu, X.W., Zhang, Y.G., 2003. The influence of tectonic deformation on some geochemical properties of coals: a possible indicator of outburst potential. Int. J. Coal Geol. 53, 69–79.

Chalmers, G.R.L., Bustin, R.M., 2007. On the effects of petrographic composition on coalbed methane sorption. Int. J. Coal Geol. 69, 288–304.

Cheng, Q.M., 1999. Multifractality and spatial statistics. Comput. Geosci. 25, 949–961.

Chhabra, A.B., Meneveau, C., Jensen, R.V., Sreenivasan, K.R., 1989. Direct determination of the $f(\alpha)$ singularity spectrum and its application to fully developed turbulence. Phys. Rev. A 40, 5284–5294.

Clarkson, C.R., Bustin, R.M., 1996. Variation in micropore capacity and size distribution with composition in bituminous coal of the Western Canadian Sedimentary Basin. Fuel 75, 1483–1498.

Clarkson, C.R., Bustin, R.M., 1999. The effect of pore structure and gas pressure upon the transport properties of coal: a laboratory and modeling study. 1. Isotherms and pore volume distributions. Fuel 78, 1333–1344.

Feder, J., 1988. Fractals. Plenum Press, New York.

Firouzi, M., Rupp, E.C., Liu, C.W., Wilcox, J., 2014. Molecular simulation and experimental characterization of the nanoporous structures of coal and gas shale. Int. J. Coal Geol. 121, 123–128.

Friesen, W.I., Mikula, R.J., 1987. Fractal dimensions of coal particles. J. Colloid Interface Sci. 120, 263–271.

Friesen, W.I., Mikula, R.J., 1988. Mercury porosimetry of coals: pore volume distribution and compressibility. Fuel 67, 1516–1520.

Frodsham, K., Gayer, R.A., 1999. The impact of tectonic deformation upon coal seams in the South Wales coalfield, UK. Int. J. Coal Geol. 38, 297–332.

Gan, H., Nandi, S.P., Walker Jr., P.L., 1972. Nature of the porosity in American coals. Fuel 51, 272–277.

Gauden, P.A., Terzyk, A.P., Rychlicki, G., 2001. The new correlation between microporosity of strictly microporous activated carbons and fractal dimension on the basis of the Polanyi–Dubinin theory of adsorption. Carbon 39, 267–278.

Giffin, S., Littke, R., Klaver, J., Urai, J.L., 2013. Application of BIB-SEM technology to characterize macropore morphology in coal. Int. J. Coal Geol. 114, 85–95.

Gökhan Şenel, I., Güniz Gürüz, A., Yücel, H., Kandas, A.W., Sarofim, A.F., 2001. Characterization of pore structure of Turkish coals. Energy Fuel 15, 331–338.

Golab, A., Ward, C.R., Permana, A., Lennox, P., Botha, P., 2013. High-resolution three-dimensional imaging of coal using microfocus X-ray computed tomography, with special reference to modes of mineral occurrence. Int. J. Coal Geol. 113, 97–108.

Grassberger, P., Procaccia, I., 1983. Characterization of strange attractors. Phys. Rev. Lett. 50, 346–349.

Guo, X.Q., Yao, Y.B., Liu, D.M., 2014. Characteristics of coal matrix compressibility: an nvestigation by mercury intrusion porosimetry. Energy Fuel 28, 3673–3678.

Hodot, B.B., 1961. Outburst of Coal and Coalbed Gas. National Mining Scientific and Technical Documentation Press. Moscow.

Hou, Q.L., Li, H.J., Fan, J.J., Ju, Y.W., Wang, T.K., Li, X.S., Wu, Y.D., 2012. Structure and coalbed methane occurrence in tectonically deformed coals. Sci. China Earth Sci. 55 (11), 1755–1763.

Kravchenko, A.N., Boast, C.W., Bullock, D.G., 1999. Multifractal analysis of soil spatial variability. Agron. J. 91, 1033–1041.

Kumar, H., Lester, E., Kingman, S., Bourne, R., Avila, C., Jones, A., Robinson, J., Halleck, P.M., Mathews, J.P., 2011. Inducing fractures and increasing cleat apertures in a bituminous coal under isotropic stress via application of microwave energy. Int. J. Coal Geol. 88, 75–82.

Lamberson, M.N., Bustin, R.M., 1993. Coalbed methane characteristics of gates formation coals, Northeastern British Columbia: effect of maceral composition. AAPG Bull. 77, 2062–2076.

Lawrie, G.A., Gentle, I.R., Fong, C., Glikson, M., 1997. Atomic force microscopy studies of Bowen Basin coal macerals. Fuel 76, 1519–1526.

Li, H.Y., 2001. Major and minor structural features of a bedding shear zone along a coal seam and related gas outburst, Pingdingshan coalfield, northern China. Int. J. Coal Geol. 47, 101–113.

Li, Y.H., Lu, G.Q., Rudolph, V., 1999. Compressibility and fractal dimension of fine coal particles in relation to pore structure characterisation using mercury porosimetry. Part. Part. Syst. Charact. 16, 25–31.

Li, H.Y., Ogawa, Y., Shimada, S., 2003. Mechanism of methane flow through sheared coals and its role on methane recovery. Fuel 82, 1271–1279.

Liu, Y.Y., Wilcox, J., 2013. Molecular simulation studies of CO_2 adsorption by carbon model compounds for carbon capture and sequestration applications. Environ. Sci. Technol. 47, 95–101.

Liu, C.Y., Zhao, Z.Y., Yang, X.K., 2000. Strong activity and active deep action: two important features of Chinese sedimentary basins. Oil Gas Geol. 21 (1), 1–6 (in Chinese with English abstract).

Mahamud, M., López, Ó., Pis, J.J., Pajares, J.A., 2003. Textural characterization of coals using fractal analysis. Fuel Process. Technol. 81, 127–142.

Mandelbrot, B.B., 1967. How long is the coast of Britain? Science 156, 636–638.

Mares, T.E., Moore, T.A., Moore, C.R., 2009. Uncertainty of gas saturation estimates in a subbituminous coal seam. Int. J. Coal Geol. 77, 320–327.

Mastalerz, M., Drobniak, A., Strąpoć, D., Solano Acosta, W., Rupp, J., 2008. Variations in pore characteristics in high volatile bituminous coals: implications for coal bed gas content. Int. J. Coal Geol. 76, 205–216.

Montero, E., Martín, M.A., 2003. Hölder spectrum of dry grain volume–size distributions in soil. Geoderma 112, 197–204.

Muller, J., 1996. Characterization of pore space in chalk by multifractal analysis. J. Hydrol. 187, 215–222.

Muller, J., McCauley, J.L., 1992. Implication of fractal geometry for fluid flow properties of sedimentary rocks. Transp. Porous Media 8, 133–147.

Neimark, A.V., 1990. Calculating surface fractal dimensions of adsorbents. Adsorpt. Sci. Technol. 7, 210–219.

Paz Ferreiro, J., Vidal Vázquez, E., 2010. Multifractal analysis of Hg pore size distributions in soils with contrasting structural stability. Geoderma 160, 64–73.

Peitgen, H., Jürgens, H., Saupe, D., 1992. Chaos and Fractals. Springer Press, New York.

Posadas, A.N.D., Giménez, D., Quiroz, R., Protz, R., 2003. Multifractal characterization of soil pore systems. Soil Sci. Soc. Am. J. 67, 1361–1369.

Prinz, D., Pyckhout-Hintzen, W., Littke, R., 2004. Development of the meso- and macroporous structure of coals with rank as analysed with small angle neutron scattering and adsorption experiments. Fuel 83, 547–556.

Qu, Z.H., Wang, G.G.X., Jiang, B., Rudolph, V., Dou, X.Z., Li, M., 2010. Experimental study on the porous structure and compressibility of tectonized coals. Energy Fuel 24, 2964–2973.

Radlinski, A.P., Mastalerz, M., Hinde, A.L., Hainbuchner, M., Rauch, H., Baron, M., Lin, J.S., Fan, L., Thiyagarajan, P., 2004. Application of SAXS and SANS in evaluation of porosity, pore size distribution and surface area of coal. Int. J. Coal Geol. 59, 245–271.

Rényi, A., 1955. On a new axiomatic theory of probability. Act. Math. Hung. 6, 285–335.

Riedi, R.H., Crouse, M.S., Ribeiro, V.J., Baraniuk, R.G., 1999. A multifractal wavelet model with application to network traffic. IEEE Trans. Inf. Theory 45, 992–1019.

Ritter, H.L., Drake, L.C., 1945. Pore-size distribution in porous materials. I. Pressure porosimeter and determination of complete macropore size distributions. Ind. Eng. Chem. Anal. Ed. 17, 782–786.

San José Martínez, F., Martín, M.A., Caniego, F.J., Tuller, M., Guber, A., Pachepsky, Y., García-Gutiérrez, C., 2010. Multifractal analysis of discretized X-ray CT images for the characterization of soil macropore structures. Geoderma 156, 32–42.

Sanjurjo-Sánchez, J., Vidal Vázquez, E., 2013. Characterizing weathering of granite buildings by multifractal analysis of mercury intrusion porosimetry. Vadose Zone J. 12 (http://dx.doi.org/10.2136/vzj2012.0204).

Shi, J.Q., Durucan, S., 2005. Gas storage and flow in coalbed reservoirs: implementation of a bidisperse pore model for gas diffusion in a coal matrix. SPE Reserv. Eval. Eng. 8, 169–175.

Sing, K.S.W., Everett, D.H., Haul, R.A.W., Moscou, L., Pierotti, R.A., Rouquérol, J., Siemieniewska, T., 1985. Reporting physisorption data for gas/solid systems with special reference to the determination of surface area and porosity. Pure Appl. Chem. 57, 603–619.

Su, X.B., Feng, Y.L., Chen, J.F., Pan, J.N., 2001. The characteristics and origins of cleat in coal from Western North China. Int. J. Coal Geol. 47, 51–62.

Suuberg, E.M., Deevi, S.C., Yun, Y., 1995. Elastic behavior of coals studied by mercury porosimetry. Fuel 74, 1522–1530.

Toda, Y., Toyoda, S., 1972. Application of mercury porosimetry to coal. Fuel 51, 199–201.

Unsworth, J.F., Fowler, C.S., Jones, L.F., 1989. Moisture in coal 2. Maceral effects on pore structure. Fuel 68, 18–26.

Vidal Vázquez, E., Paz Ferreiro, J., Miranda, J.G.V., Paz González, A., 2008. Multifractal analysis of pore size distributions as affected by simulated rainfall. Vadose Zone J. 7, 500–511.

Washburn, E.W., 1921. The dynamics of capillary flow. Phys. Rev. 17, 273–283.

Wu, D., Liu, G.J., Sun, R.Y., Chen, S.C., 2014. Influences of magmatic intrusion on the macromolecular and pore structures of coal: evidences from Raman spectroscopy and atomic force microscopy. Fuel 119, 191–201.

Xie, S.Y., Cheng, Q.M., Ling, Q.C., Li, B., Bao, Z.Y., Fan, P., 2010. Fractal and multifractal analysis of carbonate pore-scale digital images of petroleum reservoirs. Mar. Pet. Geol. 27, 476–485.

Xu, R.T., Li, H.J., Guo, C.C., Hou, Q.L., 2014. The mechanisms of gas generation during coal deformation: preliminary observations. Fuel 117, 326–330.

Yao, Y.B., Liu, D.M., 2012. Comparison of low-field NMR and mercury intrusion porosimetry in characterizing pore size distributions of coals. Fuel 95, 152–158.

Yao, Y.B., Liu, D.M., Tang, D.Z., Tang, S.H., Huang, W.H., Liu, Z.H., Che, Y., 2009a. Fractal characterization of seepage-pores of coals from China: an investigation on permeability of coals. Comput. Geosci. 35, 1159–1166.

Yao, Y.B., Liu, D.M., Tang, D.Z., Tang, S.H., Che, Y., Huang, W.H., 2009b. Preliminary evaluation of the coalbed methane production potential and its geological controls in the Weibei Coalfield, Southeastern Ordos Basin, China. Int. J. Coal Geol. 78, 1–15.

Zhang, H., 2001. Genetical type of pores in coal reservoir and its research significance. J. China Coal Soc. 26 (1), 40–44 (in Chinese with English abstract).

Zhang, B.Q., Li, S.F., 1995. Determination of the surface fractal dimension for porous media by mercury porosimetry. Ind. Eng. Chem. Res. 34, 1383–1386.

Zhang, B.Q., Liu, W., Liu, X.F., 2006. Scale-dependent nature of the surface fractal dimension for bi- and multi-disperse porous solids by mercury porosimetry. Appl. Surf. Sci. 253, 1349–1355.

Zhang, D.F., Gu, L.L., Li, S.G., Lian, P.C., Tao, J., 2013a. Interactions of supercritical CO_2 with coal. Energy Fuel 27, 387–393.

Zhang, D.F., Gu, L.L., Li, S.G., Lian, P.C., Tao, J., 2013b. Error analyses in volumetric method for measuring methane and CO_2 adsorption on coal. Int. J. Global Warming. 5, 197–209.

Zheng, Q.R., Liu, H.F., Li, W., Yao, H.F., Yan, J.W., 2015. Mercury porosimetry and small angle X-ray scattering characterization of tectonic deformation of pore structure in coals. China Min. Mag. 24 (1), 149–154 (in Chinese with English abstract).

Zou, M.J., Wei, C.T., Zhang, M., Shen, J., Chen, Y.H., Qi, Y., 2013. Classifying coal pores and estimating reservoir parameters by nuclear magnetic resonance and mercury intrusion porosimetry. Energy Fuel 27, 3699–3708.